Geophysical Research Letters

RESEARCH LETTER
10.1029/2019GL086281

A Polar Surface Eddy Obscured by Thermal Stratification

M. Porter[1], S. F. Henley[2], A. Orkney[3], H. A. Bouman[3], B. Hwang[4], E. Dumont[1], E. J. Venables[1], and F. Cottier[1,5]

[1]Scottish Association for Marine Science, Oban, UK, [2]School of GeoSciences, University of Edinburgh, Edinburgh, UK, [3]Department of Earth Sciences, University of Oxford, Oxford, UK, [4]Department of Biological and Geographical Sciences, University of Huddersfield, Huddersfield, UK, [5]Department of Arctic and Marine Biology, UiT The Arctic University of Norway, Tromsø, Norway

Key Points:
- A cold-core Barents Sea eddy shed from the Polar Frontal region is identified and its in situ properties described
- The eddy is obscured from surface SST detection, indicating an underestimation of eddy activity where estimates are derived from satellites
- Such eddies are likely to play an important role in redistributing physical and biogeochemical properties north and south of the Polar Front

Correspondence to:
M. Porter,
marie.porter@sams.ac.uk

Citation:
Porter, M., Henley, S. F., Orkney, A., Bouman, H. A., Hwang, B., Dumont, E., et al. (2020). A polar surface eddy obscured by thermal stratification. *Geophysical Research Letters*, *47*, e2019GL086281. https://doi.org/10.1029/2019GL086281

Received 20 NOV 2019
Accepted 4 MAR 2020
Accepted article online 12 MAR 2020

Abstract Mesoscale and submesoscale eddies play an important role in the distribution of heat and biogeochemical properties throughout the global oceans. Such eddies are important in the Arctic Ocean, particularly in the frontal regions, but are difficult to detect using traditional satellite-based methods. Here we use high-resolution in situ data from an underwater glider to identify a surface eddy that was masked from remote-sensing observations. We hypothesize that this masking was driven by thermal stratification driven by surface heat fluxes. The eddy was likely generated north of the Polar Front, before crossing the front and traveling south. We estimate that the observed eddy contained 4×10^{10} m^3 of Arctic Water. The observation of this eddy, masked in satellite observations of sea surface temperature, suggests a historical underestimation of the prevalence and importance of eddies in this key mixing region. The water column of the Barents Sea, one of the circumpolar Arctic seas has a seemingly simple structure. In the south, warm Atlantic Water dominates; in the north, cold Arctic Water dominates; while at their boundary, the Arctic Water overlies the Atlantic Water. In the summer, the Arctic Water is largely devoid of the nutrients required to fuel the growth of phytoplankton, which is key to maintaining life in the ocean. In contrast, the Atlantic Water is one of the primary sources of nutrient-rich water into the Arctic. In this study, we have used an underwater robotic instrument to identify a patch of Arctic Water which has been shed from the Arctic sector of the Barents Sea into the Atlantic sector. This patch of water is seen to have lower phytoplankton concentrations than the surrounding water. Due to atmospheric heating of the surface, this patch would be indistinguishable from the surrounding Atlantic Water and so would be absent for satellite observations of sea surface temperature. We suggest that this temperature masking has meant that we have previously underestimated how much water is moved within these patches in the Arctic seas.

1. Introduction

The Barents Sea is a key gateway for advection of warm Atlantic Water (AW) into the Arctic Ocean (Loeng, 1991) and the export of Arctic Water (ArW) and ice from the Arctic Ocean (Kwok, 2009). As the meeting point of these two oceanic pathways, the Barents Sea supports high biological productivity (Erga et al., 2014). This region has undergone substantial warming over recent years, with significant changes in its structure and heat content (Lind et al., 2018) as well as local ice dynamics (Comiso & Hall, 2014). In order to predict the impacts of these changes on the physical and biological processes in the region, we need to ensure that we fully understand the structure and spatial variability of the water column.

Heat, salt, and nutrients are advected into the Barents Sea, in AW (Figure 1). On the southern shelf, the AW is present at all depths, remaining mixed throughout the winter before becoming thermally stratified during summer (Harris et al., 1998). Because the thermal stratification is weak, nutrient-rich deep waters are frequently mixed to the surface, replenishing surface nutrient inventories and sustaining primary production by phytoplankton (Reigstad et al., 2002). Further north, AW is confined to intermediate depths and is overlain by cold, fresh ArW (Harris et al., 1998). This northern water is mixed during the winter resulting in nutrient-replete surface waters (Wassmann & Reigstad, 2011). However, ice melt during the summer drives early, strong salinity stratification. The surface euphotic zone becomes depleted of nutrients as a result of the export of primary production out of the surface mixed layer, while strong stratification inhibits the vertical mixing required to resupply the surface with nutrients sourced from underlying waters (Wassmann & Reigstad, 2011).

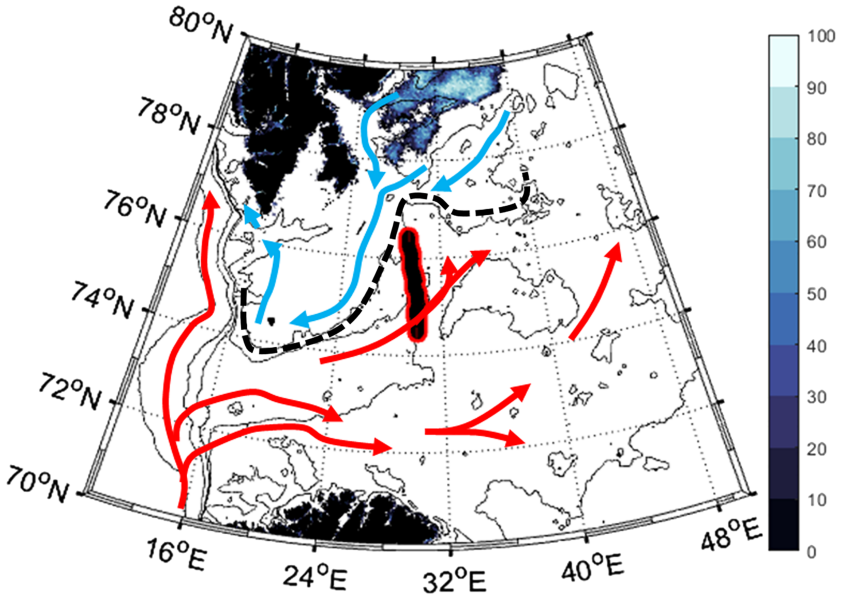

Figure 1. Map of the Barents Sea. Bathymetric data from ETOPO1 showing contours of 2,000, 1,000, 500, 350, and 200 m depth. The glider path, shown by the black/red line. A schematic of the Atlantic (red) and Arctic (blue) Water pathways, shown by colored arrows. An approximation of the location of the PF, shown by the dashed black line. The sea ice concentration (%) as observed by the AMSR 2 satellite (Saf, 2019) on 23 July 2017 is also shown.

The contrasting regions of the northern and southern Barents Sea are delineated by the Polar Front (PF) (Figure 1), which manifests as strong lateral gradients in temperature and salinity (Fer & Drinkwater, 2014; Harris et al., 1998). This boundary between water masses is subject to strong vertical mixing (Mahadevan, 2006), which enhances the supply of deep-sourced nutrients, making the PF a region of high primary production (Erga et al., 2014). Lateral transport can overcome the front, advecting nutrients, heat, salt/fresh water, and plankton between the water masses (Crews et al., 2018). Such transport relies on the breakdown of geostrophic control at the front (Huthnance, 1995) and the development of eddies and meanders that convert potential energy of the front into kinetic energy (Pingree, 1978).

Despite being localized features, eddies can have disproportionately wide impacts, influencing global circulation (e.g., Thompson et al., 2014) and biogeochemical cycles, driving enhanced carbon export (Omand et al., 2015) through their role in initiating spring blooms (Mahadevan et al., 2012). In the Arctic, horizontal advection by eddies affects nutrient transport and leads to localized phytoplankton patchiness, enhancing or limiting productivity depending on the impact on bloom conditions (Kushnir et al., 2010). Vertical transport within eddies further contributes to their significant role in Arctic biogeochemical cycles (Watanabe et al., 2014). Eddies are also important for redistributing heat across the Arctic (Hattermann et al., 2016) and ventilating subsurface waters (Crews et al., 2018).

The primary methods for quantifying the occurrence of eddies are models (Crews et al., 2018) and satellite observations of either sea surface temperature (SST) (Hausmann & Czaja, 2012), ocean color (Hausmann & Czaja, 2012) or sea surface height (SSH) (Itoh & Yasuda, 2010). However, the prevalence of cloud and rain in Arctic regions imposes limitations on using remote-sensing techniques to detect eddies from their characteristic SST and ocean color signatures. In the Barents Sea, the potentially small size of these eddies, due to the short Rossby radius of deformation (Crews et al., 2018), further exacerbates these observational difficulties, given the biased spatial resolution of the satellite data. Recently, synthetic aperture radar (SAR) has been used to address these resolution-based limitations (Atadzhanova et al., 2018; Kozlov et al., 2019). Beyond these satellite observations, in situ studies of eddies in the Barents Sea are limited, if not absent from the literature.

The use of satellite observations to estimate eddy abundance may also be limited by the presence of subsurface eddies (Kostianoy & Belkin, 1989; Manley & Hunkins, 1985) that are not detectable by remote sensing. We suggest that masking of eddies from SST and SAR imagery could be apparent in regions where there are strong atmosphere–ocean heat fluxes (Smedsrud et al., 2010), such as the Barents Sea. Thus, in regions

where estimates of eddy activity are derived largely from remote sensing, the number of eddies may be underestimated substantially due to these masked or hidden eddies. Augmenting our observations with these hidden eddies, particularly their hydrographic and biogeochemical properties, will facilitate a more complete understanding of transport pathways and their impacts on phytoplankton dynamics and allow for improvements in our estimates of primary productivity in this key biological region.

In this study, we present a unique data set obtained using an ocean glider that captures an eddy traveling southward from the PF. We combine fields of temperature, salinity, and chlorophyll-*a* fluorescence (chl-*a*) measured by the glider operating south of the PF satellite observations to evaluate the properties of the eddy in a larger spatial and temporal context. The effects of this eddy on the local chlorophyll concentrations are discussed, as well as the implications for our current understanding of eddy prevalence in the Barents Sea PF region.

2. Data sets and Methods

To investigate submesoscale–mesoscale variability and instabilities in the PF region of the Barents Sea, we deployed a glider south of the PF to sample a south–north transect along 30°E. During the period of the glider deployment, the transect was occupied by the *RRS James Clark Ross*. Observations of hydrographic properties and chl-*a* were made in order to allow for discussion of observed hydrographic features and to provide calibration profiles for the glider.

2.1. Hydrographic Data

We deployed a Slocum Glider (Webb et al., 2001), Unit 306, on 17 July 2017 to complete a transect along 30°E between 74.5°N and 76.5°N and recovered it on 31 July 2017. The glider profiled to 200 m on each dive, collecting a total of 744 profiles in a zig-zag pattern with an average profile spacing of 1 km.

The conductivity, temperature, and depth (CTD) data from the glider were processed in accordance with Garau et al. (2011) before being corrected to the calibrated temperature and salinity profiles collected from the ship at either end of the transect, on deployment, and recovery. Profiles of buoyancy frequency (N^2) along the glider transect were calculated, with the depth of maximum N^2 giving a biologically relevant proxy for the lower limit of the mixed layer (Carvalho et al., 2017).

The glider-based chl-*a* data were derived from fluorescence at wavelengths of 470/695 nm, measured by a Wetlabs triplet ECO Puck. While these values do not quantitatively represent phytoplankton biomass, they allow for the identification of spatial and temporal patterns and gradients in the phytoplankton distribution. The chl-*a* data were checked for consistency using water samples collected during the calibration profiles. Triplicate samples for chl-*a* analysis were measured onboard using the fluorometric method (Holm-Hansen et al., 1965). Between 100 and 200 ml of seawater were filtered onto 0.7 μm Whatman GF/F filter papers then extracted overnight in the dark in 90% acetone in a −20 °C freezer. Pigment extracts were then analyzed using a calibrated Trilogy fluorometer (TurnerDesigns, www.turnerdesigns.com, accessed: 2020).

The corrected, quality-controlled glider data set was gridded along the transect using a Barnes optimal analysis (Barnes, 1994) with a search radius of 4 km, representing the local Rossby radius. Due to surface and deep apogee maneuvers of the glider, we have only considered data deeper than 10 m and shallower than 190 m.

2.2. Satellite Data

Satellite-derived SST and SSH data were acquired for the duration of the glider deployment. The SST data are MURSST (Multi-scale Ultra-high Resolution Sea Surface Temperature) (Chin et al., 2017; NASA, 2019, https://podaac.jpl.nasa.gov/Multi-scale_Ultra-high_Resolution_MUR-SST, last accessed: 2020). The SSH data are delayed-mode absolute dynamic topography from Copernicus Marine Environment Monitoring Service (CMEMS, 2019, https://cds.climate.copernicus.eu/cdsapp#!/dataset/sea-level-daily-gridded-data--for-the-global-ocean-from-1993-to-present?tab=overview, last accessed: 2020). These data sets are merged products and as such are available regardless of the cloud cover. The merged SST data are a combination of low-resolution microwave data (during cloud cover or rain) and high-resolution radiometer data (during clear skies) with resolution dependant on the local weather conditions. SST and SSH data are used to

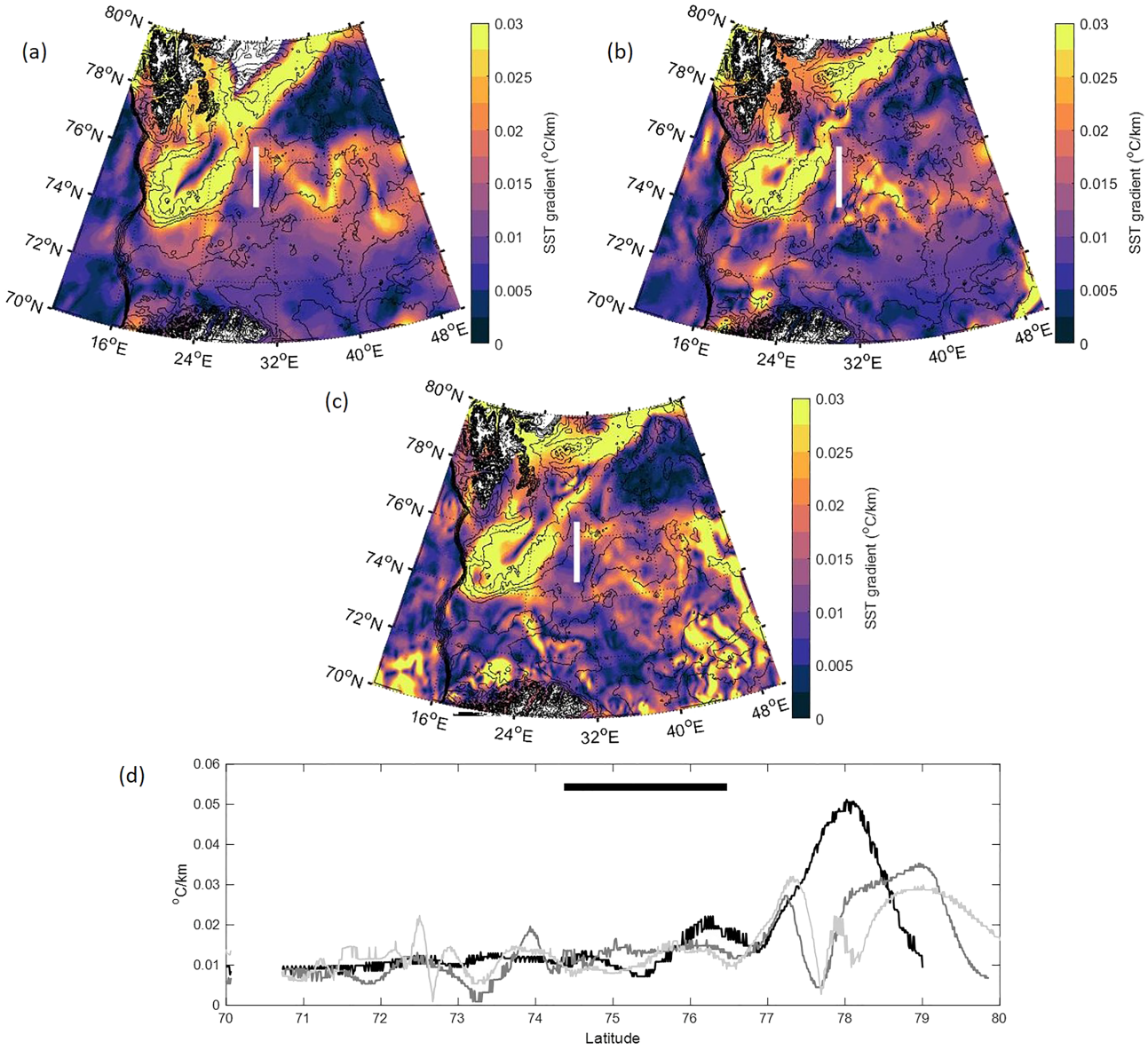

Figure 2. The SST gradient from the MURSST satellite data, plotted over the bathymetry, on 17 (a), 23 (b), and 31 (c) July 2017. (d) The magnitude of the SST gradient along the 30°E line (white line) for the three dates (black (17), dark gray (23), and light gray (31); the black bar indicates the latitudinal extent of the glider transect.

investigate surface signals of mesoscale variability and to identify the location of the PF during the glider mission. As a proxy for its location, we calculated the magnitude of the SST gradient (Barton et al., 2018) following

$$|\nabla SST| = \sqrt{(\partial SST/\partial x)^2 + (\partial SST/\partial y)^2}.$$

3. Results

3.1. The Surface Location of the PF

Throughout this study, the latitude of the surface expression of the PF in the Hopen Trough at 30°E was between 77°N and 78°N (Figure 2) although its strength and location were variable. Based on sea surface

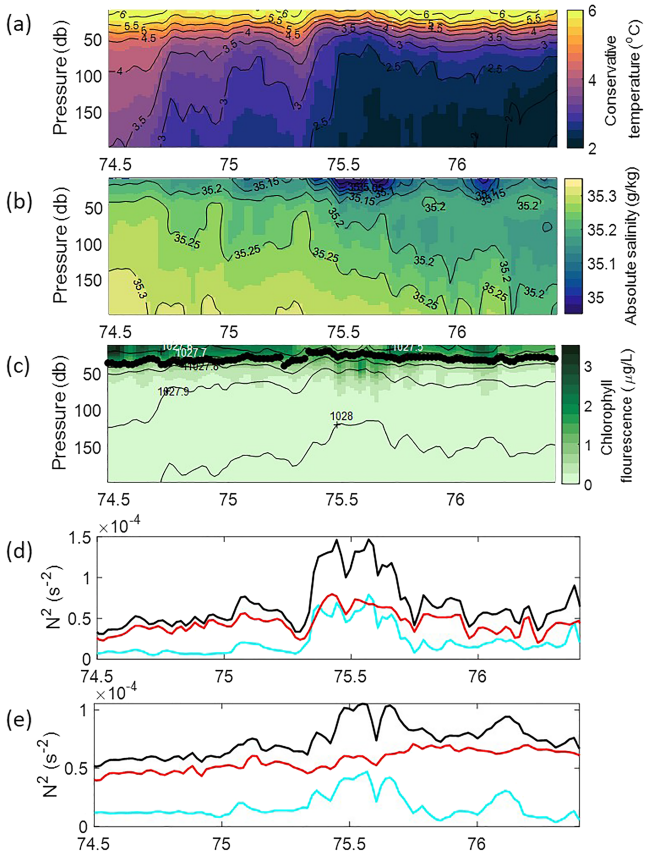

Figure 3. Gridded data from the glider transect along 30°E. (a) Conservative temperature. (b) Absolute salinity. (c) Chl-*a* with black contours of density and black dots showing the depth of the maximum buoyancy frequency (N^2). (d) Depth-averaged N^2 in the layer from surface to 20 m (black line), the contribution of salinity to this (blue line), and the contribution of temperature (red line). (e) the same as for (d) but the layer from 20 to 60 m.

gradients, we calculate that the surface expression of the PF was located more than 55 km from the northern end of the glider transect.

3.2. Water Column Variability South of the PF

The glider observations showed AW (1 °C < T < 8 °C and 35.17 g/kg < S < 35.37 g/kg (adapted from Harris et al. (1998)) dominating throughout the glider profiles (Figure 3a,b), with a shallow surface layer depth (defined as the depth of maximum N^2) of up to approximately 40 m, and strong surface stratification. Within the surface layer, measured chl-*a* concentrations were found to be higher than 2 μg/l reflecting significant phytoplankton biomass (Figure 3c). A deep incursion of colder and fresher water was found north of 75.4°N. This modified AW is evidence of mixing between ArW (T < 0 °C and 34.46 g/kg < S < 35 g/kg (adapted from Harris et al. (1998))) and AW and is indicative of the glider entering the region influenced by the PF.

Along the transect, between approximately 75.3°N and 75.7°N, the glider encountered a notable anomaly 0.02 g/kg fresher than the adjacent surface water (Figure 3b). This surface salinity feature was also identified in the temperature field but with a weaker signal 0.4 °C cooler than adjacent water (Figure 3a). This surface anomaly was tied to a colder fresh anomaly down to 100 m depth 0.7 °C and 0.02 g/kg lower than adjacent water (Figures 3a and 3b). The water within the anomaly is fresher than elsewhere on the transect, suggesting it did not have a local source. Instead, this water (T = 2.4 °C, S = 35.22 g/kg, at 100 m) lies on a mixing line between ArW and AW, indicating that it likely originated from north of the PF. The cold, fresh water covered an area with a diameter of ~30 km and a depth of ~100 m.

The anomaly shows increased N^2 in the upper water column, when compared to the rest of the transect (Figure 3d), reflecting the additional freshwater in the system. In the 0–20 m layer of the water column, the increased N^2 is driven by increased thermal stability as well as reduced salinity, while low salinity is the sole driver of increased N^2 between 20 and 60 m. The greater stability in the 0–20 m layer compared to the 20–60 m layer (Figure 3d) can be attributed to the additional thermal stratification at the surface which enhances water column stability.

Within the low-salinity, low-temperature anomaly, the surface chl-*a* concentration (0.8 μg/L) is lower than the ambient water (2.1 μg/L), and a subsurface chl-*a* maximum is observed, centered on approximately 50 m (Figure 3c). This contrasts with the rest of the glider transect, where chl-*a* concentrations were highest at the surface and decreased with depth.

4. Discussion

We have identified a cold, fresh anomaly south of the Barents Sea PF with an approximate radius of 15 km. This anomalous feature had low chl-*a* and was fresher in surface waters and colder and fresher at depth than the ambient water masses, indicating its source region as within or north of the PF. The location of this feature in otherwise warm and saline AW leads us to describe it as a cold-core eddy.

This eddy showed a surface temperature signal up to 1 °C cooler than the surrounding waters but is not detectable within the satellite SST data (Figure 4a) which has a spatial resolution of 1–35 km and a thermal resolution of 0.3–1 °C (NASA, 2019). We assume that given the structure visible in the available SST data that the time period of interest is toward the lower end of the spatial resolution of the MURSST data set. However, the eddy is observable as a slight depression in satellite SSH data (Figure 4b) which allows us to track its development/movement from the PF region toward the area where we measured it (Figure 5). We show that this eddy is thermally capped such that thermal stratification decouples the

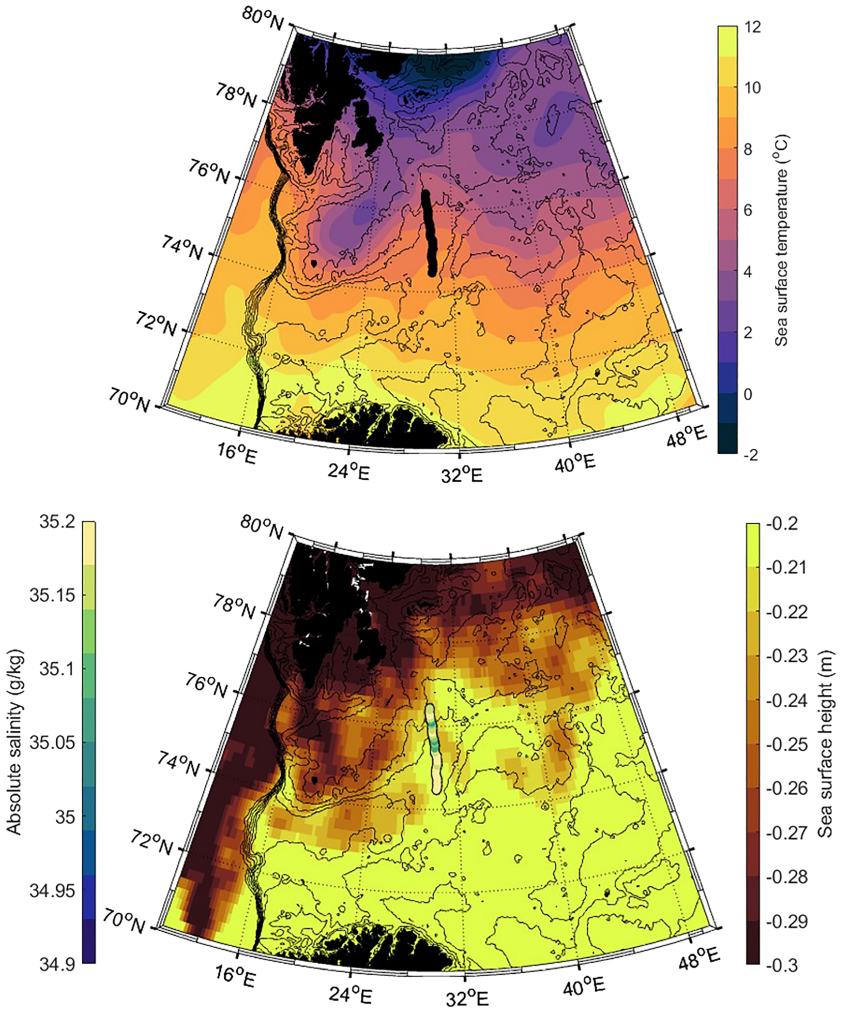

Figure 4. (a) The SST on 23 July from the MUR SST satellite product. The glider was in the cool, low salinity feature on this day. (b) The SSH (in meters) on the 23 July. The green line shows the glider transect and is colored by the absolute salinity at 30 m, showing the low salinity and low SSH feature overlapping.

thermal properties of the eddy from the surface signal (Figure 3), confounding its identification through SST.

The eddy we have described here has stronger thermally driven stability at its surface that at depth, however, we do not see a similar difference between the surface and deep haline stability (Figures 3d and 3e). If the local oceanographic conditions were driving the thermal stratification, we would expect to see a concurrent increase in salinity and a decrease in surface haline stability. We hypothesize that the change in surface thermal stability and the thermal capping of the eddy is due to local atmospheric heat fluxes.

Surface heat fluxes act over the entire region; hence, this heat input will have occurred over the entire observational area. However, in the region of the eddy, the surface fluxes act on a particularly stable patch of low salinity water, further stabilizing it. Here the energy is confined to the shallowest waters, increasing their stability. Using NCEP/NCAR reanalysis values (Kalnay et al., 1996) for latent heat (Q_{LH}), sensible heat (Q_{SH}), longwave radiation (Q_{LW}), and shortwave radiation (Q_{SW}), we can estimate the local net surface heat flux (Q_T) following

$$Q_T = Q_{SW} + Q_{LH} + Q_{SH} + Q_{LW}.$$

We use this estimate to compare the thermal properties of the observed eddy with those of a model eddy whose temperature is initially isothermal (set equal to the subthermocline temperature of 2.75 °C) and subject to the

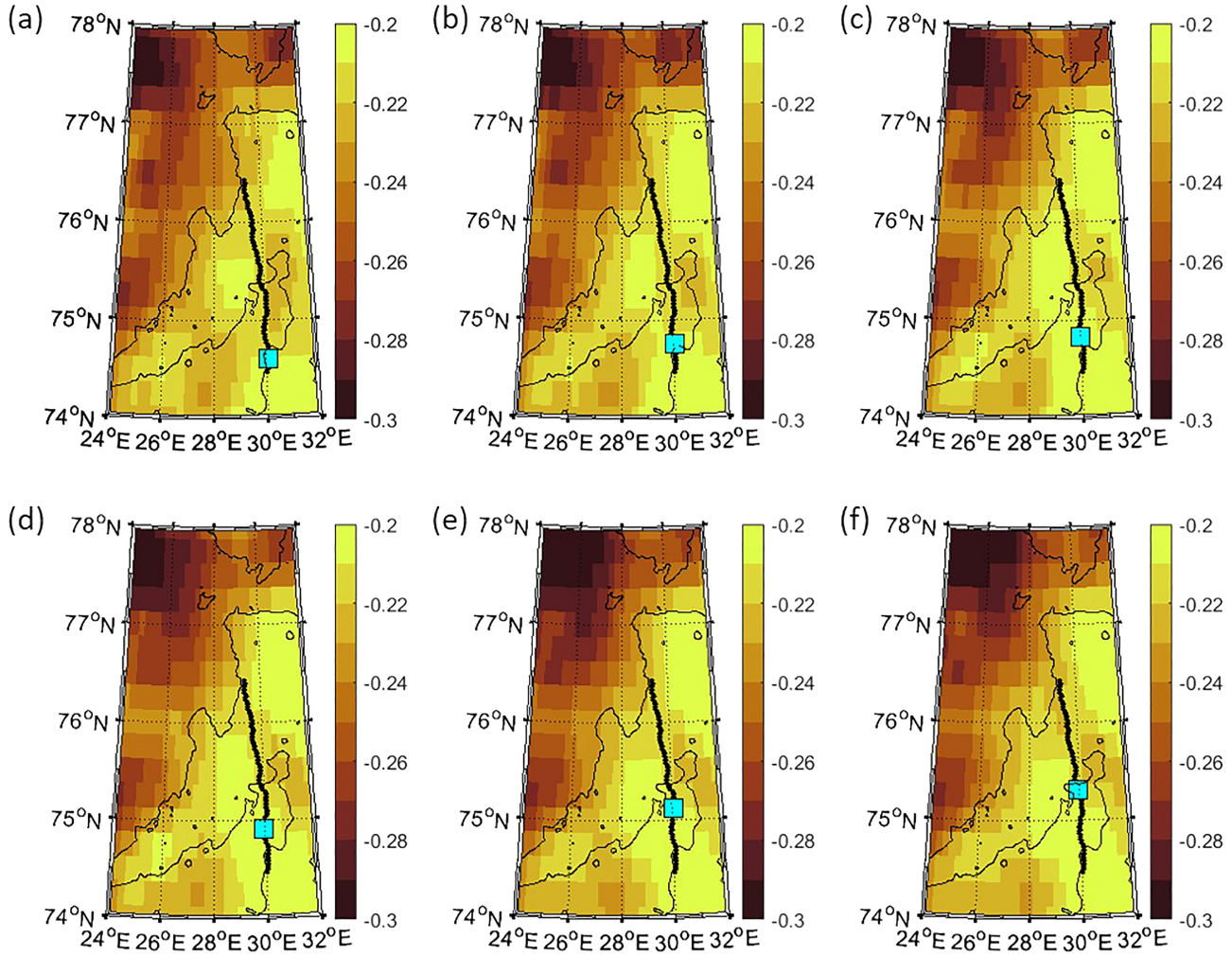

Figure 5. The SSH data in meters for 18 (a), 19 (b), 20 (c), 21 (d), 22 (e), and 23 (f) July. The black line depicts the glider track throughout its deployment, and the blue square is the location of the glider on the day shown.

NCEP/NCAR heat fluxes. Analysis of SSH data suggests that we observed the eddy approximately 5 days after its genesis (Figure 5) and so have calculated the cumulative surface heat flux experienced by the model eddy over this time. The integrated heat flux over 5 days was 190 W m^{-2} which contributed 8.2×10^7 J m^{-2} of heat energy. This would increase the heat content within the upper 60 m of the model eddy from an initial value of 6.3×10^8 J m^{-2} to a final value of 7.1×10^8 J m^{-2}. This is comparable to the maximum heat content of 8.3×10^8 J m^{-2} measured within the upper 60 m of the observed eddy. The estimate of heat content within the model eddy is subject to the eddy's initial description. The isothermal eddy is purposefully simple and provides the most conservative estimate in heat content. Any initial stratification in the source region of the eddy would act to bring the observed and modeled heat contents closer together.

The similarity of the heat contents indicates that surface warming of the observed eddy through atmospheric heat fluxes after being shed at the PF is a plausible mechanism leading to the creation of a thermal cap which would obscure the eddy from observation by satellite-derived SST. It is clear that this process will occur in tandem with restratification processes such as discussed by Bosse et al. (2019), who describe lateral heat fluxes and exchanges.

Given that satellite SST observations are limited by both resolution and depth penetration (Chin et al., 2017), we suggest that the current estimates of surface eddies in this oceanographically—and biologically—important region are low, due to both inadequate spatial resolution to capture these features and the effects of thermal capping of cold-core eddies.

The stability anomalies (Figures 3a and 3d) observed by the glider delineate the edges of the eddy, where we crossed it. If we assume that we crossed through the center of the eddy, this offers a conservative suggestion that it has a radius of approximately 15 km and a depth of 60 m, giving a total water volume of 4×10^{10} m^3. This is much larger than the local Rossby radius which is closer to 4–5 km (Nurser & Bacon, 2014), suggesting a mesoscale eddy.

Estimates from Atadzhanova et al. (2018) show that approximately 25% of the eddies in the Barents Sea occur in the region around the PF. Their estimates of the average number of cold-core eddies in 2007 and 2011, with an average diameter of 3.6 km, combined with our estimates of eddy depth (a conservative estimate of 60 m) suggest that up to 1.1×10^{13} m^3 of low-chl-*a* water could be transported to the south from the PF region each year. Given that the eddy identified in this study is both masked from detection by thermal capping and larger than those suggested by Atadzhanova et al. (2018), this is likely to be an underestimation of the total volume of this cold, fresh, potentially low nutrient water transported in eddies south of the PF during summer. Such underestimation will impact our understanding of water mass transport across the PF and its biogeochemical implications with respect to larvae distribution (Schlüter & Rachor, 2001), nutrient concentrations, and primary productivity (Kushnir et al., 2010).

The northward progression of Atlantic conditions in the Barents Sea (Lind et al., 2018) may weaken or displace the PF (Oziel et al., 2016), influencing the location and frequency of eddy genesis. The results of the present study show that such changes in the PF region may not be observable using traditional SST based approaches due to capping of surface eddies. To understand the impacts of any change in eddy activity on the transport and redistribution of heat, freshwater, nutrients, and biomass, we need to quantify the effect of surface masking on our estimates of eddy activity. The phenomenon of thermally capped eddies observed here in the Barents Sea may be applicable to all regions subject to high surface heat fluxes.

5. Summary

We used a glider, satellites, and ship-based profiles to identify and describe a thermally capped PF eddy in the Barents Sea. The water within this eddy was characterized by low surface chl-*a*. Using glider-derived estimates of the extent of the measured eddy and previous estimates of eddy size and abundance in this region (Atadzhanova et al., 2018), we have calculated a minimum annual volume transport of 1.1×10^{13} m^3 of cold, fresh low-chl-*a* water from the PF region into the Atlantic sector of the Barents Sea.

The thermal capping of this eddy and its size makes its detection by SST observations or traditional sampling methods difficult. This gives rise to the potential for historical underestimates of the occurrence of such features leading to a significant gap in our understanding of the physical biogeochemical and ecological importance of eddies within this PF region. This work has clear implications for our understanding of hydrographic variability around Polar Frontal regions and the transport of heat, salt, and nutrients across these hydrographic barriers.

Acknowledgments
This study is a contribution to the Arctic PRIZE research project (NE/P006302/1), part of the Changing Arctic Ocean program funded by the UKRI Natural Environment Research Council (NERC). We thank the crew and scientists of JR16006, for the successful cruise operations and the deployment/recovery of the glider. We also thank the NERC MARS facility for their assistance in the preparation and piloting of the glider. All of the data within this study are available from the British Oceanographic Data Centre at https://www.bodc.ac.uk/resources/inventories/edmed/report/6777/

References

Atadzhanova, O., Zimin, A., Svergun, E., & Konik, A. (2018). Submesoscale eddy structures and frontal dynamics in the Barents Sea. *Physical Oceanography*, *25*(3), 220–228. https://doi.org/10.22449/1573-160X-2018-3-220-228

Barnes, S. L. (1994). Applications of the Barnes objective analysis scheme, Part II: Improving derivative estimates. *Journal of Atmospheric and Oceanic Technology*, *11*(6), 1449–1458. https://doi.org/10.1175/1520-0426(1994)011<1449:AOTBOA>2.0.CO;2

Barton, B. I., Lenn, Y.-D., & Lique, C. (2018). Observed atlantification of the Barents Sea causes the Polar Front to limit the expansion of winter sea ice. *Journal of Physical Oceanography*, *48*(8), 1849–1866. https://doi.org/10.1175/jpo-d-18-0003.1

Bosse, A., Fer, I., Lilly, J. M., & Søiland, H. (2019). Dynamical controls on the longevity of a non-linear vortex: The case of the Lofoten Basin Eddy. *Scientific Reports*, *9*, 13448. https://doi.org/10.1038/s41598-019-49599-8

Carvalho, F., Kohut, J., Oliver, M. J., & Schofield, O. (2017). Defining the ecologically relevant mixed-layer depth for Antarctica's coastal seas. *Geophysical Research Letters*, *44*, 338–345. https://doi.org/10.1002/2016GL071205

Chin, T. M., Vazquez-Cuervo, J., & Armstrong, E. M. (2017). A multi-scale high-resolution analysis of global sea surface temperature. *Remote Sensing of Environment*, *200*, 154–169. https://doi.org/10.1016/j.rse.2017.07.029

Comiso, J. C., & Hall, D. K. (2014). Climate trends in the Arctic as observed from space. *Wiley Interdisciplinary Reviews: Climate Change*, *5*(3), 389–409. https://doi.org/10.1002/wcc.277

Crews, L., Sundfjord, A., Albretsen, J., & Hattermann, T. (2018). Mesoscale eddy activity and transport in the Atlantic Water inflow region north of Svalbard. *Journal of Geophysical Research: Oceans*, *123*, 201–215. https://doi.org/10.1002/2017jc013198

Erga, S. R., Ssebiyonga, N., Hamre, B., Frette, Ø., Rey, F., & Drinkwater, K. (2014). Nutrients and phytoplankton biomass distribution and activity at the Barents Sea Polar Front during summer near Hopen and Storbanken. *Journal of Marine Systems*, *130*, 181–192. https://doi.org/10.1016/j.jmarsys.2012.12.008

Fer, I., & Drinkwater, K. (2014). Mixing in the Barents Sea Polar Front near Hopen in spring. *Journal of Marine Systems*, *130*, 206–218. https://doi.org/10.1016/j.jmarsys.2012.01.005

Garau, B., Ruiz, S., Zhang, W. G., Pascual, A., Heslop, E., Kerfoot, J., & Tintoré, J. (2011). Thermal lag correction on Slocum CTD glider data. *Journal of Atmospheric and Oceanic Technology*, *28*(9), 1065–1071. https://doi.org/10.1175/JTECH-D-10-05030.1

Harris, C. L., Plueddemann, A. J., & Gawarkiewicz, G. G. (1998). Water mass distribution and polar front structure in the western Barents Sea. *Journal of Geophysical Research*, *103*(C2), 2905–2917. https://doi.org/10.1029/97JC02790

Hattermann, T., Isachsen, P. E., von Appen, W.-J., Albretsen, J., & Sundfjord, A. (2016). Eddy-driven recirculation of Atlantic Water in Fram Strait. *Geophysical Research Letters*, *43*, 3406–3414. https://doi.org/10.1002/2016gl068323

Hausmann, U., & Czaja, A. (2012). The observed signature of mesoscale eddies in sea surface temperature and the associated heat transport. *Deep Sea Research Part I: Oceanographic Research Papers*, *70*, 60–72. https://doi.org/10.1016/j.dsr.2012.08.005

Holm-Hansen, O., Lorenzen, C. J., Holmes, R. W., & Strickland, J. D. (1965). Fluorometric determination of chlorophyll. *ICES Journal of Marine Science*, *30*(1), 3–15. https://doi.org/10.1093/icesjms/30.1.3

Huthnance, J. M. (1995). Circulation, exchange and water masses at the ocean margin: the role of physical processes at the shelf edge. *Progress in Oceanography*, *35*(4), 353–431. https://doi.org/10.1016/0079-6611(95)80003-C

Itoh, S., & Yasuda, I. (2010). Characteristics of mesoscale eddies in the Kuroshio–Oyashio Extension region detected from the distribution of the sea surface height anomaly. *Journal of Physical Oceanography*, *40*(5), 1018–1034. https://doi.org/10.1175/2009jpo4265.1

Kalnay, E., Kanamitsu, M., Kistler, R., Collins, W., Deaven, D., Gandin, L., et al. (1996). The NCEP/NCAR 40-year reanalysis project. *Bulletin of the American Meteorological Society*, *77*(3), 437–471. https://doi.org/10.1175/1520-0477(1996)077<0437:TNYRP>2.0.CO;2

Kostianoy, A., & Belkin, I. (1989). A survey of observations on intrathermocline eddies in the world ocean. In J. C. J. Nihoul & B. M. Jamart (Eds.), *Elsevier oceanography series* (pp. 821–841). Elsevier.

Kozlov, I. E., Artamonova, A. V., Manucharyan, G. E., & Kubryakov, A. A. (2019). Eddies in the Western Arctic Ocean from spaceborne SAR observations over open ocean and marginal ice zones. *Journal of Geophysical Research: Oceans*, *124*, 6601–6616. https://doi.org/10.1029/2019jc015113

Kushnir, V., Pavlov, V., Morozov, A., & Pavlova, O. (2010). Flashes of chlorophyll-a concentration derived from in situ and remote sensing data at the Polar Front in the Barents Sea. *Open Oceanography Journal*, *4*, 14–21. https://doi.org/10.2174/1874252101105010014

Kwok, R. (2009). Outflow of Arctic Ocean sea ice into the Greenland and Barents Seas: 1979–2007. *Journal of Climate*, *22*(9), 2438–2457. https://doi.org/10.1175/2008jcli2819.1

Lind, S., Ingvaldsen, R. B., & Furevik, T. (2018). Arctic warming hotspot in the northern Barents Sea linked to declining sea-ice import. *Nature Climate Change*, *8*(7), 634–639. https://doi.org/10.1038/s41558-018-0205-y

Loeng, H. (1991). Features of the physical oceanographic conditions of the Barents Sea. *Polar Research*, *10*(1), 5–18. https://doi.org/10.3402/polar.v10i1.6723

Mahadevan, A. (2006). Modeling vertical motion at ocean fronts: Are nonhydrostatic effects relevant at submesoscales? *Ocean Modeling*, *14*(3–4), 222–240. https://doi.org/10.1016/j.ocemod.2006.05.005

Mahadevan, A., D'Asaro, E., Lee, C., & Perry, M. J. (2012). Eddy-driven stratification initiates North Atlantic spring phytoplankton blooms. *Science*, *337*(6090), 54–58. https://doi.org/10.1126/science.1218740

Manley, T. O., & Hunkins, K. (1985). Mesoscale eddies of the Arctic Ocean. *Journal of Geophysical Research*, *90*(C3), 4911–4930. https://doi.org/10.1029/JC090iC03p04911

NASA (2019), https://podaac.jpl.nasa.gov/Multi-scale_Ultra-high_Resolution_MUR-SST last accessed: 2020.

Nurser, A. J. G., & Bacon, S. (2014). The Rossby radius in the Arctic Ocean. *Ocean Science*, *10*(6), 967–975. https://doi.org/10.5194/os-10-967-2014

Omand, M. M., D'Asaro, E. A., Lee, C. M., Perry, M. J., Briggs, N., Cetinić, I., & Mahadevan, A. (2015). Eddy-driven subduction exports particulate organic carbon from the spring bloom. *Science*, *348*(6231), 222–225. https://doi.org/10.1126/science.1260062

Oziel, L., Sirven, J., & Gascard, J. C. (2016). The Barents Sea frontal zones and water masses variability (1980–2011). *Ocean Science*, *12*(1), 169–184. https://doi.org/10.5194/os-12-169-2016

Pingree, R. (1978). Cyclonic eddies and cross-frontal mixing. *Journal of the Marine Biological Association of the United Kingdom*, *58*(4), 955–963. https://doi.org/10.1017/S0025315400056885

Reigstad, M., Wassmann, P., Wexels Riser, C., Øygarden, S., & Rey, F. (2002). Variations in hydrography, nutrients and chlorophyll a in the marginal ice-zone and the central Barents Sea. *Journal of Marine Systems*, *38*(1), 9–29. https://doi.org/10.1016/S0924-7963(02)00167-7

Saf, O. (2019). Sea ice concentration product (OSI-401-b) of the EUMETSAT Ocean and Sea Ice Satellite Application Facility (www.osi-saf.org).

Schlüter, M., & Rachor, E. (2001). Meroplankton distribution in the central Barents Sea in relation to local oceanographic patterns. *Polar Biology*, *24*(8), 582–592. https://doi.org/10.1007/s003000100255

Smedsrud, L. H., Ingvaldsen, R., Nilsen, J. E. Ø., & Skagseth, Ø. (2010). Heat in the Barents Sea: Transport, storage, and surface fluxes. Ocean Science, *6*, 219–234. https://doi.org/10.5194/os-6-219-2010

Thompson, A. F., Heywood, K. J., Schmidtko, S., & Stewart, A. L. (2014). Eddy transport as a key component of the Antarctic overturning circulation. *Nature Geoscience*, *7*(12), 879–884. https://doi.org/10.1038/ngeo2289, https://www.nature.com/articles/ngeo2289#supplementary-information

Wassmann, P., & Reigstad, M. (2011). Future Arctic Ocean seasonal ice zones and implications for pelagic-benthic coupling. *Oceanography*, *24*(3), 220–231. https://doi.org/10.5670/oceanog.2011.74

Watanabe, E., Onodera, J., Harada, N., Honda, M. C., Kimoto, K., Kikuchi, T., et al. (2014). Enhanced role of eddies in the Arctic marine biological pump. *Nature Communications*, *5*, 3950. https://doi.org/10.1038/ncomms4950

Webb, D. C., Simonetti, P. J., & Jones, C. P. (2001). SLOCUM: An underwater glider propelled by environmental energy. *IEEE Journal of Oceanic Engineering*, *26*(4), 447–452. https://doi.org/10.1109/48.972077